Strain-induced competition between ferromagnetism and emergent antiferromagnetism in (Eu,Sr)MnO$_3$

A. J. Grutter,[1] S. M. Disseler,[1] E. J. Moon,[2] D. A. Gilbert,[1,3] E. Arenholz,[4] A. Suter,[5] T. Prokscha,[5]
Z. Salman,[5] B. J. Kirby,[1] and S. J. May[2]

[1]*NIST Center for Neutron Research, National Institute of Standards and Technology, Gaithersburg, Maryland 20899, USA*
[2]*Materials Science and Engineering, Drexel University, Philadelphia, Pennsylvania 19104, USA*
[3]*Materials Science and Engineering, University of Tennessee, Knoxville, Tennessee 37996, USA*
[4]*Advanced Light Source, Lawrence Berkeley National Laboratory, Berkeley, California 94720, USA*
[5]*Laboratory for Muon-Spin Spectroscopy, Paul Scherrer Institute, CH-5232 Villigen PSI, Switzerland*

(Received 24 April 2018; revised manuscript received 29 June 2018; published 4 September 2018)

We demonstrate emergent antiferromagnetic interactions in strained thin films of the mixed valence manganite (Eu,Sr)MnO$_3$. Although the composition studied, Eu$_{0.7}$Sr$_{0.3}$MnO$_3$, will nominally yield a ferromagnetic phase in the bulk, we observe significant suppression of the saturation magnetization in films under both tensile and compressive strain. Despite the magnetization suppression, muon spin rotation spectrometry and polarized neutron reflectometry reveal uniform magnetic ordering in these films. Neutron diffraction and x-ray absorption spectroscopy demonstrate high-temperature G-type antiferromagnetic order in films under tensile strain, in contrast to the A- and C-type orders that are found in the phase diagrams of bulk (Eu,Sr)MnO$_3$ and other mixed-valence manganites. These probes also show that compressive strain results in a uniform but suppressed magnetization suggestive of moment canting resulting from competition between ferromagnetism and antiferromagnetism.

DOI: 10.1103/PhysRevMaterials.2.094402

The rich electronic and magnetic phase diagrams exhibited by transition-metal oxides make them ideal candidates through which to explore fundamental physics and material properties [1–3]. Strong electron correlations in these systems give rise to multiple, often unexpected, pathways toward controlling magnetic and electronic ground states. Perovskite oxide thin films in particular are noted for their emergent behavior and extreme tunability, which has led to considerable interest in identifying control parameters that can unlock functional device applications [4–6].

More specifically, there is extensive interest in the identification of mechanisms that allow deterministic switching between distinct magnetic phases or, in mixed phase systems, modifying relative magnetoelectronic phase fractions. Both Mn- and Co-based oxides are well known for hosting multiple magnetic structures in close compositional proximity and for magnetoelectronic phase separation, which plays an important role in establishing interesting properties such as colossal magnetoresistance and magnetoelectronic coupling [4,7–12]. Epitaxial strain is among the most successful tools for modifying the magnetic and electronic ground state of perovskites such as the cobaltites and manganites [13,14]. These systems are sensitive to a wide variety of strain states, and they exhibit responses varying from simple tetragonal distortions to more complex modifications of tilt and rotation patterns of the oxygen octahedra [15–18].

The mixed-valence manganite Eu$_{0.7}$Sr$_{0.3}$MnO$_3$ (ESMO) shows a strong potential for strain engineering of its electronic and magnetic phases due to its narrow Mn e_g bandwidth, which has been associated with close competition among ground states in related systems such as Pr$_{1-x}$Sr$_x$MnO$_3$, Sm$_{1-x}$Sr$_x$MnO$_3$, and Nd$_{1-x}$Sr$_x$MnO$_3$ [19–23]. Manganites based on the closest 4f elemental neighbors of Eu—Sm$_{0.7}$Sr$_{0.3}$MnO$_3$ and Gd$_{0.7}$Sr$_{0.3}$MnO$_3$—are ferromagnetic (FM) and antiferromagnetic (AFM), respectively [21,24]. Thus, ESMO is likely situated very near a stability boundary between several magnetically ordered phases.

Indeed, thin films of ESMO exhibit several classic signatures of competing order and possible magnetoelectronic phase separation. Purely FM ESMO films are expected to exhibit a nominal Mn$^{3.3+}$ valence and a corresponding saturation magnetization of 3.7μ_B/Mn. Indeed, Moon *et al.* achieve a saturation magnetization of 3.3μ_B/Mn by growing ESMO on a (LaAlO$_3$)$_{0.3}$(Sr$_2$AlTaO$_6$)$_{0.7}$ (LSAT) substrate [19]. LSAT substrates induce only a small strain (+0.58%) on the ESMO film, while larger applied strains (compressive or tensile) result in a drastic reduction of the saturation magnetization [19]. Specifically, growth on LaAlO$_3$ (LAO), SrLaAlO$_4$, and SrTiO$_3$ (STO) yields saturation magnetizations of 2.1μ_B/Mn, 1.8μ_B/Mn, and 0.4μ_B/Mn, respectively. One may suspect that certain strain states alter oxygen stoichiometry inducing a change in Mn valence [25,26] and thus suppressing FM, but x-ray absorption spectroscopy (XAS) probes demonstrate that the Mn valence is constant across strain states. Strain-induced magnetoelectronic phase segregation incorporating magnetically disordered or AFM regions may instead explain these observations. Alternatively, competition between AFM and FM order may yield a canted ground state and suppress the magnetization even in a uniformly ordered film.

In this work, we demonstrate that the strain-induced magnetization suppression in ESMO films is consistent with strong competition between multiple forms of magnetic ordering and the emergence of a G-type AFM phase. First, we use low-energy muon spin rotation spectroscopy (μSR) to extract the magnetically ordered phase fractions of strained ESMO films under 1.5% compressive strain (on LAO) and 1.5% tensile strain (on STO). The μSR results demonstrate that the entire films are magnetically ordered regardless of the observed magnetization, and they provide evidence of an emergent magnetic phase with a transition temperature far above the approximately 70 K Curie temperature (T_C) of unstrained ESMO. Mn valence information and element-specific magnetic information are obtained through XAS while magnetic depth profiles are extracted with polarized neutron reflectometry (PNR). Finally, G-type AFM ordering with a Néel temperature of 203 K (T_N, 95% confidence interval of 159–225 K) is specifically identified within the ESMO film on STO through neutron diffraction.

For the purposes of this study, the samples of greatest interest exhibit significant magnetization suppression. Informed by the previous results of Moon *et al.*, we therefore probed ESMO films grown on LAO (ESMO/LAO) and STO (ESMO/STO) with nominal thicknesses of 40 unit cells (≈16 nm) [19]. As discussed above, films on LAO are reported to saturate at a magnetization of approximately 2.1μ_B/Mn while films on STO exhibit only trace FM with a saturated moment of less than 0.4μ_B/Mn. Samples were fabricated using molecular beam epitaxy as described in Ref. [19], and they are in fact the same samples used for the study in Ref. [19].

I. LOW-ENERGY MUON SPIN ROTATION SPECTROSCOPY

Low-energy muons are ideal for interrogating the magnetic uniformity within the ESMO films. In low-energy μSR experiments, a spin-polarized muon with kinetic energy of 0.5–20 keV is implanted in a material, where it decays and emits a positron and a pair of neutrinos. The positron is preferentially emitted along the spin direction of the muon, so that examining the directional asymmetry of the positron emission as a function of time can provide insight into the magnetic ordering of the material. Because the muon is sensitive only to the local field, muons that stop in a nonmagnetic region experience a very different environment from those that stop in an ordered region, enabling elucidation of magnetic phase fractions.

The low implantation energies necessary in thin films limit time-resolution so that high-frequency asymmetry contributions from magnetically ordered regions are smeared out and effectively go “missing” [27]. Thus, the experiments are performed in a small applied magnetic field so that only magnetically disordered regions contribute to the asymmetry. One can then determine the magnetic phase fraction by fitting the muon decay asymmetry with the function

$$A(t,T) = A_0(T)\,e^{-\lambda(T)t}\cos(\omega_L t), \tag{1}$$

where $A_0(T)$ is the initial asymmetry measured at the temperature T, λ is the depolarization rate, and $\omega_L = \gamma_\mu B_{\text{ext}}$ is the Larmor precession frequency at the applied field $B_{\text{ext}} = \mu_0 H_{\text{ext}}$. The magnetically ordered phase fraction is $f_{\text{M}} = 1 - A_0(T)/A_0(T \gg T_{\text{M}})$, with $A_0(T \gg T_{\text{M}})$ being the maximal asymmetry in the paramagnetic phase and T_{M} being the magnetic transition temperature. Although μSR can probe magnetic phase fractions, differentiating between FM versus AFM generally requires other techniques.

Extracting magnetic phase fractions from measurements performed in the absence of an applied field is less precise, but such zero-field measurements allow more accurate extraction of the muon depolarization rate. In this case the functional dependence for the zero-field muon polarization can be modeled by

$$A(t,T) = A_0^{\text{ZF}}(T)\exp[-\lambda_{\text{ZF}}(T)t], \tag{2}$$

where $A_0^{\text{ZF}}(T)$ is the zero-field asymmetry and $\lambda_{\text{ZF}}(T)$ is the corresponding depolarization rate. A peak in $\lambda_{\text{ZF}}(T)$ is expected at the magnetic transition due to the critical slowing down of magnetic fluctuations, allowing T_C or T_N to be identified [28].

Low-energy μSR measurements were performed at the LEM beamline [29] of the Swiss Muon Source for ESMO/LAO and ESMO/STO in a temperature range of 10–180 K. All the muSR data were analyzed by MUSRFIT [30]. Measurements were performed at zero field and in a 10 mT field applied normal to the film surface, with the initial muon spin parallel to the sample surface ([100] direction). Samples were field-cooled (when applicable) with measurements made on cooling. The muon implantation depth was tuned by varying the incident kinetic energy, and the expected implantation depth profiles were calculated with the Monte Carlo code TRIM.SP [31]. ESMO/LAO was measured at implantation energies of 1 and 2 keV, corresponding to an implantation depth of 5 ± 4 nm ($\geqslant$98% muons in film) and 12 ± 5 nm (≈78% muons in film), respectively, with the stopping profiles shown in Fig. 1(a). Unless otherwise noted, all uncertainties represent ±1 standard deviation. In the ESMO/STO case, implantation in STO results in muonium formation at approximately 60 K, potentially leading to a large extrinsic change in muon depolarization near the T_C of ESMO [32]. We avoid these complications by examining only a 1 keV implantation energy so that the majority of the muons stop in the ESMO.

We first examine λ_{ZF} of 1 keV muons implanted into an ESMO/LAO film at temperatures ranging from 10 to 120 K, shown in Fig. 1(b). A weak peak is observed in λ_{ZF} at the expected T_C of 70 K, in agreement with the expected FM-to-paramagnetic transition temperature. However, the large uncertainty in this peak requires confirmation of the T_C by examining the asymmetry with and without an applied field. For both field conditions and energies, the ESMO/LAO sample also exhibits the 70 K T_C, with a clear increase in the asymmetry at this temperature, as shown in Figs. 1(c) and 1(d). In contrast, Figs. 1(c) and 1(d) show no sharp transition in $A_0(T)$ across T_C for the ESMO/STO sample, which exhibits a plateau below approximately 65 K, followed by a monotonic increase up to at least 160 K. This is a strong indication of emergent magnetic order, which persists to at least 160 K within the ESMO/STO film. Since the μSR is sensitive to both FM and AFM order, the nature of this magnetic phase is not immediately apparent. However, the lack of an observed magnetization in ESMO/STO films suggests the stabilization of AFM.

To examine magnetoelectronic phase separation and quantify the ordered and disordered phase fractions of ESMO/LAO and ESMO/STO, we focus on the measurements performed at 10 mT, shown in Fig. 1(d). We note that, after A_0 has been corrected to account for the background from muons reflected from the surface, the asymmetry of both films is

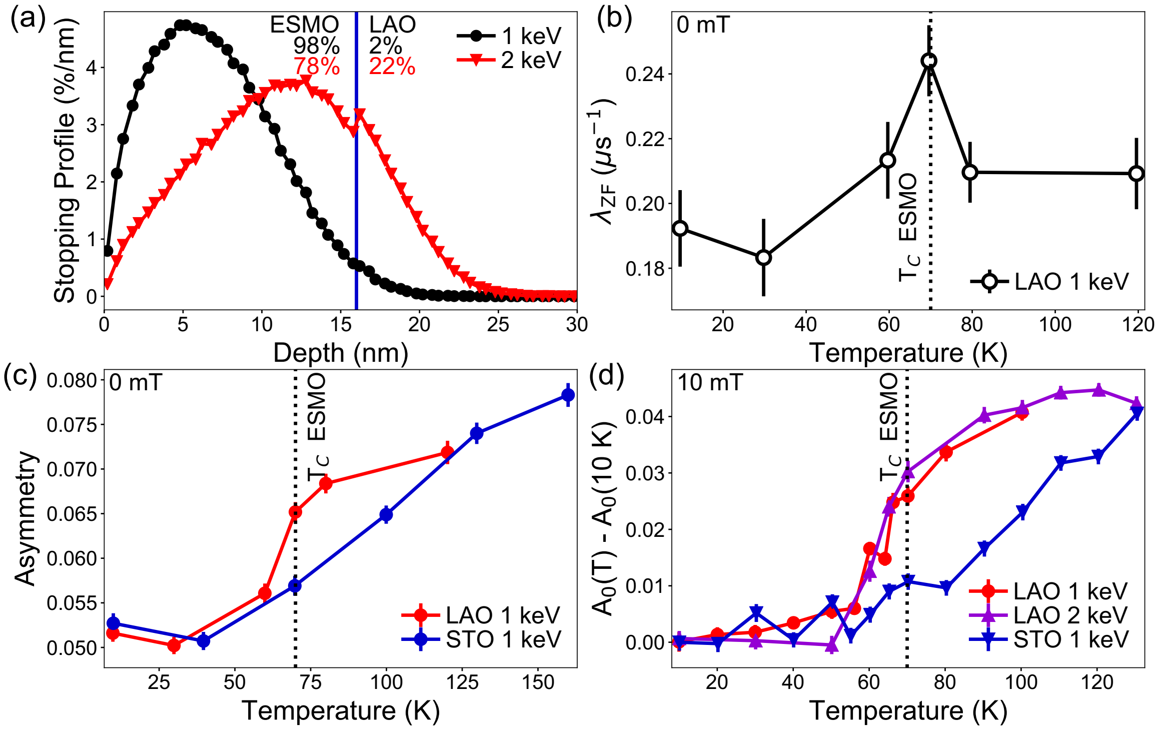

FIG. 1. (a) Normalized stopping profile for 1 and 2 keV muons incident on ESMO/LAO. (b) Zero-field muon depolarization rate as a function of temperature for muons incident on an ESMO/LAO film. (c) Zero-field asymmetry vs temperature for 1 keV muons incident on ESMO/LAO and ESMO/STO films in zero field. (d) Corrected, transverse field muon spin asymmetry, $A(T)$-$A(10\text{ K})$, vs temperature for 1 and 2 keV muons incident on ESMO/LAO and ESMO/STO films in an applied field of 10 mT.

within an uncertainty of zero at 10 K, and therefore we refer simply to the normalized asymmetry $A(T)$-A $(T = 10$ K). This indicates that both films are fully magnetically ordered at low temperature. Further, the asymmetry plateaus immediately above and below T_C for ESMO/LAO indicate constant magnetically ordered volume fractions and suggest a fully disordered paramagnetic state above T_C. These observations preclude the possibility that the magnetization reduction in ESMO/LAO is the result of nonmagnetic regions, such as those that might result from the magnetoelectronic phase separation common to mixed-valence manganites. Instead, we suggest that the most likely remaining explanation is a long-range canted magnetic spin texture in ESMO/LAO.

As stated above, ESMO/STO must also be fully ordered magnetically, although in this case the increase in A_0 with temperature is gradual rather than sharp. Such a continuous variation in magnetically ordered volume during cooling may indicate the formation of AFM puddles with a variety of Néel temperatures rather than a single uniform phase.

Thus, we conclude that the entirety of both ESMO/LAO and ESMO/STO films are magnetically ordered at 10 K. Combined with the single sharp transition in ESMO/LAO, the μSR indicates that the magnetic ground state consists of a single FM phase in which the reduced magnetization results from moment canting. On the other hand, the near-complete suppression of any net magnetization in ESMO/STO indicates that the magnetic ground state at 10 K consists of an entirely AFM film. Surprisingly, no signs of magnetoelectronic phase separation are observed in ESMO/LAO, while the broad transition observed in ESMO/STO may indicate some level of magnetic phase separation, with at least some fraction of the AFM order surviving above 160 K.

II. POLARIZED NEUTRON REFLECTOMETRY

To further confirm the homogeneity of the magnetization within the ESMO/LAO, we investigated the depth dependence of the FM through PNR. Measurements were performed using the PBR (Polarized Beam Reflectometer) instrument at the NIST Center for Neutron Research. The ESMO/LAO film was cooled to 10 K in an applied in-plane field of 700 mT, and the reflected intensity of the incident neutron beam was collected as a function of the momentum transfer (Q) normal to the film surface. Incident and scattered neutrons were polarized spin-up or spin-down with respect to the applied magnetic field. The reflected intensity of the non-spin-flip cross sections, shown in Fig. 2(a), is sensitive to both the structural depth profile and the depth profile of the magnetization parallel to the applied field. Thus, the nuclear and magnetic scattering length density (SLD) depth profiles may be extracted. PNR data were modeled using the REFL1D software package for χ^2 optimization.

The structural and magnetic depth profiles that result from fitting the PNR curves are shown in Fig. 2(b). To properly describe the data, a small ($\approx$2 nm thick) region of reduced magnetization is required at the top ESMO surface. Below this dead layer, a relatively uniform net magnetic moment of 1.2 μ_B/Mn is observed throughout the ESMO/LAO. PNR is in agreement with the μSR measurements, showing that the majority of the ESMO/LAO is uniformly FM, with a significantly smaller magnetization than the bulk.

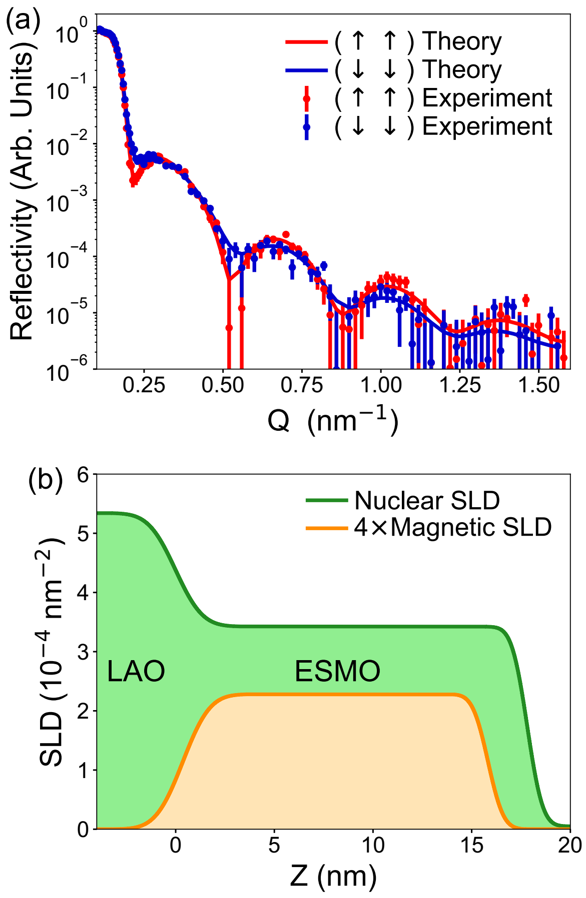

FIG. 2. (a) Fitted polarized neutron reflectometry measurement of ESMO/LAO and (b) the resulting structural and magnetic depth profiles. All error bars represent ±1 standard deviation.

III. MAGNETIC X-RAY ABSORPTION SPECTROSCOPY

To better understand the emergent magnetic phases in ESMO/STO, we probed the element-specific chemical and magnetic properties of ESMO using Mn L-edge XAS, x-ray magnetic circular dichroism (XMCD), and x-ray linear dichroism (XLD) at beamline 4.0.2 at the Advanced Light Source. Based on the muon and magnetometry results, we expect a much higher proportion of non-FM ordering in ESMO on STO, and consequently we focused on these samples. Measurements were performed at 300 and 20 K in both total electron yield (TEY) and fluorescence yield (FY) modes. Due to the difference in probing depths for photoelectrons and x rays, TEY and FY modes reflect the characteristics of the top ≈5 nm and >40 nm, respectively.

In addition to the difference in probing depths, FY XAS measurements are typically distorted by both "saturation" effects, in which a significant fraction of the incident beam is absorbed by the sample, and "self-absorption" effects, in which x rays emitted by Mn ions are reabsorbed by their neighbors [33]. These effects act to distort the line shapes of the XAS, XMCD, and XLD, particularly at the L_3 edge, which is typically strongly suppressed in FY measurements. Thus, although a great deal of qualitative information may be extracted, care must be taken when comparing TEY and FY measurements. Representative results of the x-ray spectroscopy measurements are shown in Fig. 3.

Figure 3(a) shows TEY XAS and XMCD for ESMO/STO. Weak XMCD is observed, with a peak difference between the two x-ray polarizations of about 0.05 relative to a Mn L_3 intensity of 1.0. As in previous magnetometry measurements, this dichroism indicates net magnetization far less than the magnitude expected in single-phase FM manganites, which can yield differences in excess of 0.4. However, the XAS measurements of the Mn L_2 and L_3 edges are consistent with past reports of mixed $\mathrm{Mn}^{3+}/\mathrm{Mn}^{4+}$, implying a Mn spin configuration with a magnetic moment near the expected $3.7\mu_B/\mathrm{Mn}$ even in ESMO/STO samples, which show minimal magnetization [34–36]. Thus, this magnetization suppression cannot be explained in terms of an increased (lower-moment) Mn valence.

The emergent magnetically ordered phase is therefore concluded to be predominantly AFM in nature, which should result in a nonzero XLD signal. However, nonzero XLD may also be the result of orbital polarization. In fact, the XLD present at 300 K is a close match to other reported examples of preferential $e_g(3z^2\text{-}r^2)$ occupation common to mixed valence manganite surfaces [37]. We have therefore attempted to remove the orbital polarization effects by subtracting the XLD at 300 K from the XLD at 20 K. Taking into account that the AFM order has a Néel temperature below 300 K (see additional measurements discussed below) and that the μSR saturates below 65 K, we expect a significant difference in the XLD after the temperature is lowered to 20 K. Figure 3(e) shows typical TEY XLD measurements at 300 and 20 K alongside the difference of the two (offset for clarity). Equivalent measurements in FY mode are shown in Fig. 3(f). Both modes (and therefore both surface and bulk ESMO) exhibit significant differences between high- and low-temperature XLD, suggesting a magnetic contribution. The spectral shape of the FY XA and XLD signal at the L_2 edge exhibits a similar minus/plus feature while, as expected, the L_3 edge of the XA signal measured in FY is too distorted by "self-absorption" effects to allow a meaningful comparison with the TEY data. Although a net magnetization could also produce a magnetic linear dichroism effect, it is unlikely that such a small net magnetization would do so. Since XLD arising from a net magnetization is sensitive to the application of an external field, we compared field-cooled (400 mT) and zero-field-cooled XLD measurements [38]. This comparison resulted in identical line shapes, pointing toward the presence of AFM order in the film.

We therefore conclude that the x-ray spectroscopy supports a picture in which the substrate-induced strain suppresses the FM in ESMO/STO through a transition to AFM spin alignment. Alternative explanations such as a large valence shift are inconsistent with the XAS line shapes, as previously reported.

IV. NEUTRON DIFFRACTION

Finally, we extracted the AFM spin structure of ESMO/STO directly using neutron diffraction performed with the SPINS and BT4 triple-axis spectrometer instruments at the NIST Center for Neutron Research with λ = 4.702 and 2.359 Å,

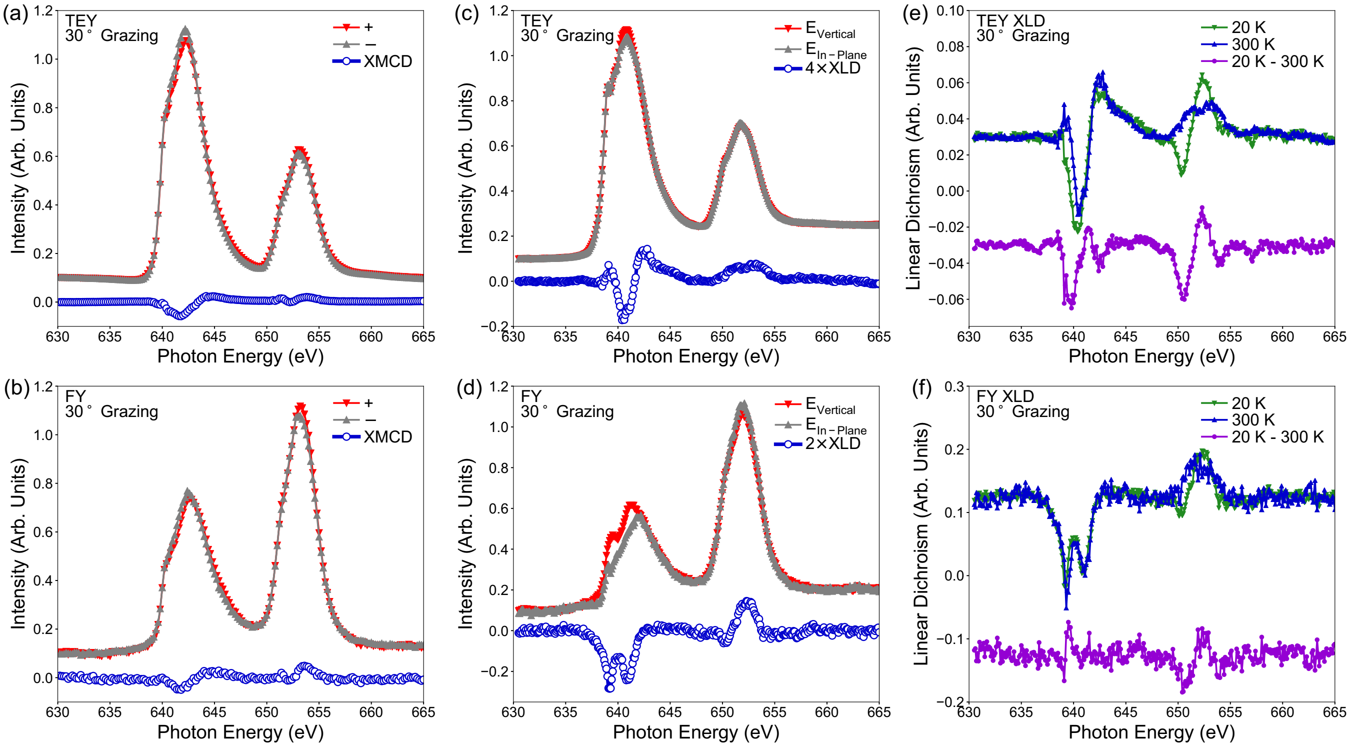

FIG. 3. (a) Total electron yield and (b) fluorescence yield x-ray absorption spectra and magnetic circular dichroism for ESMO/STO at 20 K. (c) Total electron yield and (d) fluorescence yield x-ray absorption spectra and linear dichroism for ESMO/STO at 300 K. (e) Comparison of total electron yield linear dichroism at 20 K (green) and 300 K (blue) alongside the difference (purple), which has been offset for clarity. (f) Comparison of fluorescence yield linear dichroism at 20 K (green) and 300 K (blue) alongside the difference (purple), which has been offset for clarity.

respectively. Due to the magnetic nature of the neutron, it will be scattered by the ordered magnetic moments associated with an AFM phase, yielding magnetic diffraction peaks from which the AFM spin structure can be determined. Extreme care was taken to remove all possible λ/n components from the beam using cooled Be or PG filters before and after the sample. The ratio of residual $\lambda/2$ to λ was better than 10^{-6} on both instruments. This was verified by measuring the scattering rate at the $HKL = (\frac{1}{2}, \frac{1}{2}, \frac{1}{2})$ STO reflection at room temperature, with and without filters. No detectable signal above background was observed when all filters were in place. An analyzer crystal was used to select the energy of the diffracted beam so that the observed scattering was purely elastic.

For all neutron diffraction measurements, the a (3.905 Å), b (3.905 Å), and c (3.77 Å) lattice parameters for strained ESMO/STO were taken from Ref. [19], as the nuclear reflections from ESMO were not distinguishable from the STO substrate. Samples were mounted onto single-crystal Si in both He gas and vacuum atmospheres with identical results. We probed the reciprocal space scattering vectors associated with the pseudocubic $(\frac{1}{2}, \frac{1}{2}, \frac{1}{2})$, $(0, 0, \frac{1}{2})$, $(\frac{1}{2}, \frac{1}{2}, 0)$, or $(1, 0, \frac{1}{4})$ Bragg reflections, arising from G-type, A-type, and C-type AFM order, respectively. A magnetic peak, shown in Fig. 4(a), was observed at 10 K only at the $(\frac{1}{2}, \frac{1}{2}, \frac{1}{2})$ position. As shown in Fig. 4(a), this peak was found to disappear only above 200 K, indicating it is unrelated to either the STO structural distortion at 105 K or the ESMO T_C at 70 K. Measurements of the $(\frac{1}{2}, \frac{1}{2}, \frac{1}{2})$ peak intensity (I) as a function of temperature can be fit with a function of the form

$$\begin{aligned} I &= I_0\left(1-\frac{T}{T_N}\right)^{2\beta}, \quad T < T_N, \\ I &= 0 \quad T \geqslant T_N \end{aligned} \tag{3}$$

to extract a Néel temperature of 204 ± 15 K, shown in Fig. 4(b).

V. DISCUSSION

G-type AFM ordering is a new and completely unexpected addition to the already rich magnetic and electronic phase diagram of bulk ESMO, which includes both A- and C-type AFM order in addition to the FM and spin-glass states [39–41]. In fact, either increasing *or* decreasing the Sr content of $Eu_{0.7}Sr_{0.3}MnO_3$ is expected to yield A-type AFM [39–41]. The G-type AFM order in strained ESMO/STO films therefore represents a true emergent magnetic phase with no corresponding behavior in the bulk. This spin structure requires AFM coupling across all nearest-neighbor Mn-O-Mn interactions. We postulate that along the c axis, AFM interactions are to be expected under tensile strain, which acts to depopulate the $3z^2$-r^2 orbitals leading to AFM full t_{2g}-t_{2g} interactions. Previous work has confirmed that tensile strain does promote out-of-plane AFM interactions in mixed-valent manganites, for example leading to A-type AFM in strained films that otherwise exhibit a different magnetic ordering in compositionally equivalent bulk forms [42].

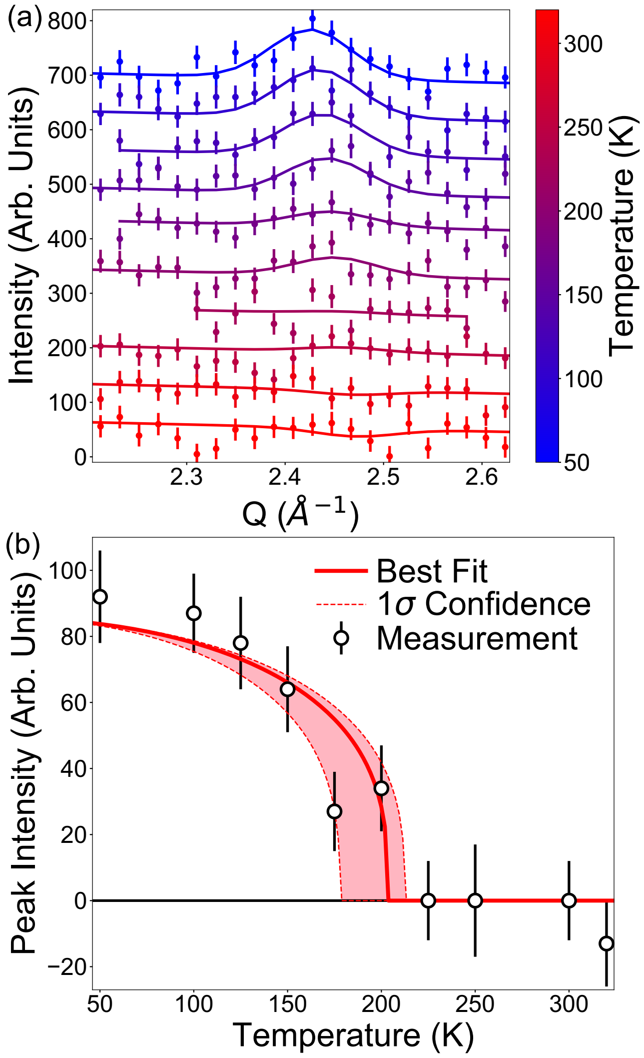

FIG. 4. (a) Neutron diffraction measurements along the [111] direction and their fit analysis showing the Q dependence through the $(\frac{1}{2}, \frac{1}{2}, \frac{1}{2})$ film peak of ESMO/STO for temperatures from 50 to 325 K. (b) Peak intensity from (a) as a function of temperature with the best fit of the order parameter (red line) and a 1σ T_N confidence interval on the temperature dependence of the $(\frac{1}{2}, \frac{1}{2}, \frac{1}{2})$ peak (shaded red region). All error bars represent ±1 standard deviation.

The origin of the in-plane AFM interactions in ESMO/STO is less clear as the mixed valence state will lead to AFM e_g^1-e_g^1 and FM e_g^1-e_g^0 interactions within the plane. Detailed theoretical studies are needed to provide insight, but we speculate that the dominance of superexchange AFM interactions is due to the reduction of in-plane bandwidth associated with the strain-induced elongation of the Mn-O bonds. The kinetic energy gain associated with double exchange is mitigated as the carriers are localized, thus favoring global AF interactions as opposed to FM within each layer. As such AFM interactions require highly insulating films, it should be noted that these ESMO films have resistivities that are several orders of magnitude higher than that of (La,Sr)MnO_3 at room temperature. Further, they exhibit the exponential temperature dependence expected of an insulator [19]. Alternatively, it is also possible that charge ordering effects such as those observed to create a canted state in closely related systems such as in $Gd_{0.7}Sr_{0.3}MnO_3$ play an important role in determining the final magnetic ground state [43]. Further investigation is clearly warranted to understand the mechanisms driving the emergent AFM order.

VI. CONCLUSIONS

In this work, we have employed μSR, soft x-ray spectroscopy, neutron diffraction, and neutron reflectometry to understand the evolution of the magnetic ground state in epitaxial ESMO films as a function of strain. While relatively unstrained films are FM with a Curie temperature of 90 K, we find that under 1.5% compressive strain the films exhibit a uniform suppressed magnetic moment of $1.2\,\mu_B$/Mn in an applied field of 700 mT that is consistent with noncollinear magnetic order such as a strongly canted AFM state. Surprisingly, μSR reveals that the magnetization suppression in ESMO/LAO cannot be attributed to phase-separated paramagnetic regions. This is also true of films under 1.5% tensile strain, where we find an emergent strain-induced G-type AFM state with $T_N = 204 \pm 15$ K, while alternative spin structures such as A- or C-type AFM are ruled out. In the ESMO/STO films, a broad AFM-to-paramagnetic phase transition may be a signature of some phase separation leading to a continuum of Néel temperatures, although this could not be definitively determined. These results highlight the sensitivity of magnetic ordering within narrow-bandwidth mixed-valence manganites to small perturbations in the Mn-O-Mn bonds.

ACKNOWLEDGMENTS

The Advanced Light Source is supported by the Director, Office of Science, Office of Basic Energy Sciences, of the U.S. Department of Energy under Contract No. DE-AC02-05CH11231. E.J.M. and S.J.M. were supported by the Army Research Office, Grant No. W911NF-15-1-0133. The muon measurements were performed at the Swiss Muon Source SμS, Paul Scherrer Institute, Villigen, Switzerland. We thank William Ratcliff II and Leland Harriger for assistance with the neutron diffraction measurements.

A.J.G. and S.M.D. contributed equally to this work.

---

[1] Y. Tokura and N. Nagaosa, Science **288**, 462 (2000).
[2] Y. Tokura and Y. Tomioka, J. Magn. Magn. Mater. **200**, 1 (1999).
[3] D. D. Stauffer and C. Leighton, Phys. Rev. B **70**, 214414 (2004).
[4] M. Uehara, S. Mori, C. H. Chen, and S.-W. Cheong, Nature (London) **399**, 560 (1999).
[5] A. Ohtomo and H. Y. Hwang, Nature (London) **427**, 423 (2004).
[6] C. He, A. J. Grutter, M. Gu, N. D. Browning, Y. Takamura, B. J. Kirby, J. A. Borchers, J. W. Kim, M. R. Fitzsimmons, X. Zhai, V. V. Mehta, F. J. Wong, and Y. Suzuki, Phys. Rev. Lett. **109**, 197202 (2012).

[7] A. Tebano, C. Aruta, P. G. Medaglia, F. Tozzi, G. Balestrino, A. A. Sidorenko, G. Allodi, R. De Renzi, G. Ghiringhelli, C. Dallera, L. Braicovich, and N. B. Brookes, Phys. Rev. B **74**, 245116 (2006).

[8] A. Tovstolytkin, A. Pogorily, A. Vovk, D. Podyalovskii, I. Lezhnenko, and A. Matviyenko, J. Magn. Magn. Mater. **272**, 1839 (2004).

[9] J. Wu and C. Leighton, Phys. Rev. B **67**, 174408 (2003).

[10] M. A. Torija, M. Sharma, J. Gazquez, M. Varela, C. He, J. Schmitt, J. A. Borchers, M. Laver, S. El-Khatib, and C. Leighton, Adv. Mater. **23**, 2711 (2011).

[11] J. Walter, H. Wang, B. Luo, C. D. Frisbie, and C. Leighton, ACS Nano **10**, 7799 (2016).

[12] P. P. Orth, R. M. Fernandes, J. Walter, C. Leighton, and B. I. Shklovskii, Phys. Rev. Lett. **118**, 106801 (2017).

[13] A. Bhattacharaya and S. J. May, Annu. Rev. Mater. Res. **44**, 65 (2014).

[14] C. Adamo, X. Ke, H. Q. Wang, H. L. Xin, T. Heeg, M. E. Hawley, W. Zander, J. Schubert, P. Schiffer, D. A. Muller, L. Maritato, and D. G. Schlom, Appl. Phys. Lett. **95**, 112504 (2009).

[15] L. M. Berndt, V. Balbarin, and Y. Suzuki, Appl. Phys. Lett. **77**, 2903 (2000).

[16] A. J. Grutter, F. J. Wong, C. A. Jenkins, E. Arenholz, A. Vailionis, and Y. Suzuki, Phys. Rev. B **88**, 214410 (2013).

[17] J. M. Rondinelli, S. J. May, and J. W. Freeland, MRS Bull. **37**, 261 (2012).

[18] A. J. Grutter, A. Vailionis, J. A. Borchers, B. J. Kirby, C. L. Flint, C. He, E. Arenholz, and Y. Suzuki, Nano Lett. **16**, 5647 (2016).

[19] E. J. Moon, D. J. Keavney, and S. J. May, Phys. Rev. Appl. **1**, 054006 (2014).

[20] Y. Tomioka, A. Asamitsu, H. Kuwahara, Y. Moritomo, and Y. Tokura, Phys. Rev. B **53**, R1689 (1996).

[21] C. Martin, A. Maignan, M. Hervieu, and B. Raveau, Phys. Rev. B **60**, 12191 (1999).

[22] V. Yu. Ivanov, A. A. Mukhin, V. D. Travkin, A. S. Prokhorov, and A. M. Balbashov, J. Magn. Magn. Mater. **258–259**, 535 (2003).

[23] R. Kajimoto, H. Yoshizawa, H. Kawano, H. Kuwahara, Y. Tokura, K. Ohoyama, and M. Ohashi, Phys. Rev. B **60**, 9506 (1999).

[24] J. S. Zhou, H. Q. Yin, J. B. Goodenough, Y. Gim, and Q. X. Jia, Appl. Phys. Lett. **75**, 1146 (1999).

[25] U. Aschauer, R. Pfenninger, S. M. Selbach, T. Grande, and N. A. Spaldin, Phys. Rev. B **88**, 054111 (2013).

[26] R. U. Chandrasena, W. Yang, Q. Y. Lei, M. U. Delgado-Jaime, K. Wijesekara, M. Golalikhani, B. A. Davidson, E. Arenholz, K. Kobayashi, M. Kobata, F. M. F. de Groot, U. Aschauer, N. A. Spaldin, X. X. Xi, and A. X. Gray, Nano Lett. **17**, 794 (2017).

[27] S. R. Dunsiger, J. P. Carlo, T. Goko, G. Nieuwenhuys, T. Prokscha, A. Suter, E. Morenzoni, D. Chiba, Y. Nishitani, T. Tanikawa, F. Matsukura, H. Ohno, J. Ohe, S. Maekawa, and Y. J. Uemura, Nat. Mater. **9**, 299 (2010).

[28] A. Yaouanc and P. Dalmas de Réotier, *Muon Spin Rotation, Relaxation, and Resonance* (Oxford University Press, Oxford, 2011).

[29] T. Prokscha, E. Morenzoni, K. Deiters, F. Foroughi, D. George, R. Kobler, A. Suter, and V. Vrankovic, Nucl. Instrum. Methods Phys. Res. Sec. A **595**, 317 (2008).

[30] A. Suter and B. M. Wojek, Phys. Proc. **30**, 69 (2012).

[31] W. Eckstein, *Computer Simulation of Ion-Solid Interactions* (Springer, Berlin, 1991).

[32] Z. Salman, T. Prokscha, A. Amato, E. Morenzoni, R. Scheuermann, K. Sedlak, and A. Suter, Phys. Rev. Lett. **113**, 156801 (2014).

[33] S. Eisebitt, T. Böske, J.-E. Rubensson, and W. Eberhardt, Phys. Rev. B **47**, 14103 (1993)

[34] J.-H. Park, E. Vescovo, H.-J. Kim, C. Kwon, R. Ramesh, and T. Venkatesan, Phys. Rev. Lett. **81**, 1953 (1998).

[35] J. J. Kavich, M. P. Warusawithana, J. W. Freeland, P. Ryan, X. Zhai, R. H. Kodama, and J. N. Eckstein, Phys. Rev. B **76**, 014410 (2007).

[36] I. Hallsteinsen, M. Moreau, A. Grutter, M. Nord, P.-E. Vullum, D. A. Gilbert, T. Bolstad, J. K. Grepstad, R. Holmestad, S. M. Selbach, A. T. N'Diaye, B. J. Kirby, E. Arenholz, and T. Tybell, Phys. Rev. B **94**, 201115 (2016).

[37] A. Tebano, C. Aruta, S. Sanna, P. G. Medaglia, G. Balestrino, A. A. Sidorenko, R. De Renzi, G. Ghiringhelli, L. Braicovich, V. Bisogni, and N. B. Brookes, Phys. Rev. Lett. **100**, 137401 (2008).

[38] C. Aruta, C. Adamo, A. Galdi, P. Orgiani, V. Bisogni, N. B. Brookes, J. C. Cezar, P. Thakur, C. A. Perroni, G. De Filippis, V. Cataudella, D. G. Schlom, L. Maritato, and G. Ghiringhelli, Phys. Rev. B **80**, 140405 (2009).

[39] Y. Tomioka, R. Kumai, T. Ito, and Y. Tokura, Phys. Rev. B **80**, 174414 (2009).

[40] Y. Tadokoro, Y. J. Shan, T. Nakamura, and S. Nakamura, Solid State Ion. **108**, 261 (1998).

[41] H. C. Ku, C. T. Chen, and B. N. Lin, J. Magn. Magn. Mater. **272**, 85 (2004).

[42] Y. Konishi, Z. Fang, M. Izumi, T. Manako, M. Kasai, H. Kuwahara, M. Kawasaki, K. Terakura, and Y. Tokura, J. Phys. Soc. Jpn. **68**, 3790 (1999).

[43] L. K. Joy, S. Thomas, and M. R. Anantharaman, J. Magn. Magn. Mater. **398**, 174 (2016).